JOURNAL OF MAGNETIC RESONANCE **124,** 218–222 (1997)
ARTICLE NO. MN961005

Optimal Detection of Weak $^nJ(^1H-^{119}Sn)$ Couplings by Gradient-Enhanced 1D and 2D Heteronuclear Multiple-Quantum Correlation Spectroscopy. Application to a Novel Tin Derivative of Erythromycin A

JOSÉ C. MARTINS,*,† FRANÇOIS KAYSER,*,‡,§ PATRICIA VERHEYDEN,* MARCEL GIELEN,‡ RUDOLPH WILLEM,*,‡ AND MONIQUE BIESEMANS*,‡

**High Resolution NMR Centre, HNMR, Room 9G621, and ‡Unit of General and Organic Chemistry of the Faculty of Engineering, AOSC, Room 8G508, Vrije Universiteit Brussel, Pleinlaan 2, B-1050 Brussels, Belgium*

Received September 9, 1996

Over the past years, organotin chemistry has enjoyed increasing interest as a source of new compounds with potential applications both in biomedicine (*1*) and in material sciences (*2*). As a result, there is a growing need for their fine-tuned structural characterization. To this end, high-resolution NMR provides powerful $^1H-\{^1H\}$ and $^1H-\{^{13}C\}$ correlation techniques (*3*), which can be supplemented by 1D ^{119}Sn NMR. Whereas their combined use furnishes a wealth of structural and conformational information as to the organic moieties in these compounds, they generally underperform as far as the characteristics of their tin atom(s) are concerned.

Although it is a main-group element, its location in the fifth period implies that the tin atom has both a highly polarizable valence-electron shell and empty 5*d* orbitals facilitating coordination extension (*4*). This high coordination variability, which extends typically from coordination four to seven for organotin(IV) compounds, is reflected by the frequent existence of intramolecular donor–acceptor interactions involving the tin atom as a Lewis acid (*4*). These interactions often lie at the frontier of real covalent bonds and strong van der Waals interactions, being characterized by bond lengths ranging from 2.4 to 3.2 Å (*5, 6*). As a consequence, while readily observable in the solid state by X-ray diffraction techniques, hypervalent organotin compounds being often crystallization friendly (*5, 6*), such intramolecular coordinations are sometimes difficult to demonstrate in solution. Doing so, however, is essential, because the same organotin compound can display different coordination features and, henceforth, different structures in the solid and solution states (*5–7*).

Although helpful, ^{119}Sn chemical-shift data are usually not sufficient to characterize the compounds (*8, 9*). The detection of weak $^nJ(^1H-^{119}Sn)$ scalar couplings is one of the tools which can provide information on weak intramolecular coordinations involving tin. Unfortunately, these couplings are hardly measurable either from standard 1D ^1H spectra, the coupling satellites being hidden in the foot of the parent ^1H resonance, or from ^{119}Sn spectra, because of the usual large linewidth of the ^{119}Sn resonances.

To address these problems, we have recently introduced 1D and 2D $^1H-\{^{119}Sn\}$ HMQC spectroscopy (*10, 11*). In our hands, this novel tool has proved essential for gaining fine structural features in a variety of organotin compounds (*12–14*). While ^{119}Sn has a more favorable natural abundance than ^{13}C (8.7 vs 1.1%), subtraction artifacts originating from phase cycling generate t_1 noise bands at the frequency of intense resonances from, for instance, *tert*-butyl or phenyl moieties. This hampers the reliable observation of $^nJ(^1H-^{119}Sn)$ scalar-coupling correlations with low intensity. This report presents and discusses the successful implementation of pulsed field gradients (PFGs) in order to overcome this dynamic-range-related drawback. The superior performance of the gradient-enhanced scheme and its impact on the structural characterization of bio-organotin compounds are demonstrated with $Ery(OSn(tBu)_2)_2O$, a novel derivative of the antibiotic erythromycin A (further represented as $Ery(OH)_2$), currently under our investigation.

Usually, three PFGs are incorporated into the basic HMQC pulse sequence to achieve the desired coherence-pathway selection (*15, 16*) (Fig. 1). Two PFGs symmetrically sandwich the $\pi(^1H)$ pulse in the center of the t_1 evolution period and the third immediately follows the last heteronuclear $\pi/2$ (^nX) pulse. The coherence-transfer pathways leading to the desired correlations, described by single-shift-transition operators (*17*), are shown in Fig. 1. After the preparation period, tuned to the $^nJ(^1H-^{119}Sn)$ couplings of interest, the first $\pi/2(^nX)$ pulse creates zero- and double-quantum coherence. Assuming I^- single-quantum coherence (SQC) is detected, the only pathways to be considered start

† To whom correspondence should be addressed.
§ Present address: Goodyear Technical Research Center—Luxembourg, Avenue Gordon Smith, L-7750 Colmar-Berg, Luxembourg.

1090-7807/97 $25.00

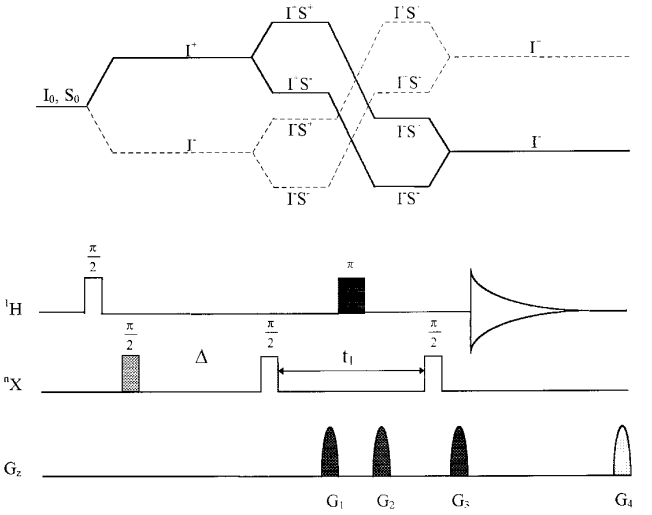

FIG. 1. Coherence pathways and pulse sequence (bottom) for gradient-enhanced HMQC spectroscopy (ge-HMQC). The coherences of interest evolving between RF pulses are labeled with the corresponding single-transition shift operators, the sign of which corresponds to the associated coherence order. G_1, G_2, and G_3 denote the gradients needed to select the coherence pathways shown as solid lines. The additional G_4 gradient may be added to avoid a gradient-recalled echo over two scans (see text). Insertion of a low-pass filter (shown dashed) yields the ge-HMBC experiment.

from I^+ SQC. In the first pathway, I^+S^+ double-quantum coherence (DQC) is converted into I^-S^+ zero-quantum coherence (ZQC) by the $\pi(^1H)$ pulse, and subsequently transformed back into I^- SQC for detection. Taking into account the negative gyromagnetic ratio of ^{119}Sn, this pathway generates the so-called anti-echo or P-type signal. The echo or N-type signal is generated from the I^+S^- (ZQC) $\rightarrow$ I^-S^- (DQC) $\rightarrow$ I^- pathway. For each pathway, the respective gradient-selection conditions are (*18*)

$$(\gamma_H + \gamma_X)G_1 + (\gamma_X - \gamma_H)G_2 - \gamma_H G_3 = 0 \quad \text{(P type)}$$

$$(\gamma_H - \gamma_X)G_1 - (\gamma_H + \gamma_X)G_2 - \gamma_H G_3 = 0 \quad \text{(N type)}.$$

As no set of gradients G_1:G_2:G_3 provides a simultaneous solution for both equations, either the P- or N-type signals will be recorded in one scan, leading to phase modulation in t_1. Choosing the G_1 and G_3 gradient strengths in a 50:40 ratio, and using 26.752 rad s^{-1} T^{-1} and -9.971 rad s^{-1} T^{-1} for γ_H and $\gamma_X = \gamma^{119}Sn$, a relative G_2 gradient strength of -6.291 or 45.65 is required to refocus the P- or N-type signal, respectively.

The performance of each of these gradient trains in refocusing exclusively the desired coherence pathway was assessed with various preparation delays from 1D ge-$^1H-\{^{119}Sn\}$ HMQC spectra (Fig. 2), recorded from concentrated triphenyltin hydride (Ph_3SnH) in C_6D_6. This sample is particularly suited because each of the ^{119}Sn satellites of the hydride proton resonance is approximately 225 times less intense than the overlapping meta and para proton resonances of the phenyl groups (Fig. 2a). Also, the large $^1J(^1H-^{119}Sn)$ of 1935 Hz gives rise to coupling satellites in empty areas of the proton spectrum, enabling convenient ^{119}Sn $\pi/2$-pulse calibration using ^1H detection via the standard $\pi/2$ (^1H)—$1/[2^nJ(^1H-^{119}Sn)]$—$\pi/2(^{119}Sn)$ sequence (*19*).

Clearly, the artifacts at the frequency of the parent ^1H signals due to incomplete subtraction in the regular phase-cycled HMQC experiment (Fig. 2b) are completely absent when gradient selection is applied instead (Fig. 2c), indicating that the coherence-transfer pathways involving non-^{119}Sn-coupled protons are efficiently dephased. As a result, the long-range $^nJ(^1H-^{119}Sn)$ couplings to the aromatic proton resonances (Fig. 2c) become observable, even after the relatively short $1/[2^1J(^1H-^{119}Sn)]$ preparation time. The particularly poor subtraction in the phase-cycled experiment can be traced back, at least in part, to the high intensity of the phenyl proton resonances of Ph_3SnH, as compared to the hydride resonance, and to external sources beyond our control.

In principle, the proposed gradient trains will leave all

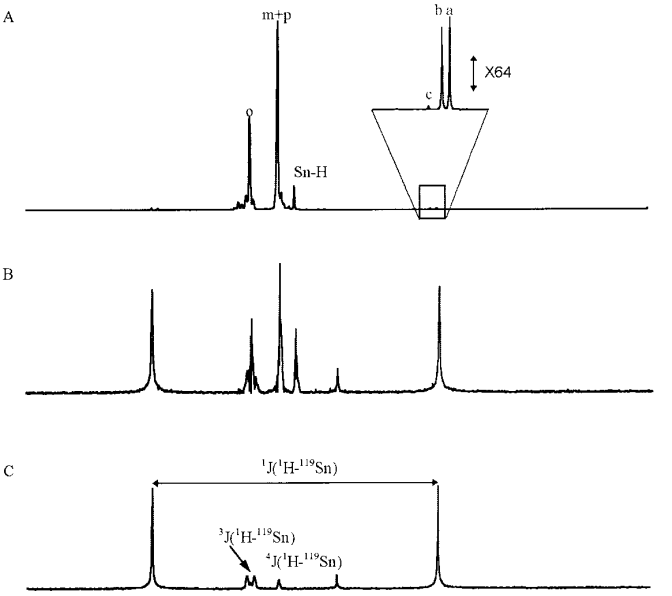

FIG. 2. Performance of the 1D ge-$^1H-\{^{119}Sn\}$ HMQC scheme demonstrated on a concentrated sample of triphenyltin hydride in C_6D_6. All experiments were recorded on a Bruker AMX500 equipped with a digital lock system and a modified TBI-Z probe and consisted of either four scans (a, b) or one scan (c) preceded by four dummy scans. Relaxation delay was 2 s, preparation delay 258 μs [tuned to $^1J(^1H-^{119}Sn)$], with 8K data points for the FID and no zero filling. Gradient strengths are expressed in percent of the maximum gradient strength of 0.62 $T.m^{-1}$, afforded by our Bruker BGU unit. FIDs were multiplied by squared cosine windows prior to Fourier transformation. (a) Reference 1D spectrum. The low-frequency tin satellites corresponding to isotopes ^{119}Sn, ^{117}Sn, and ^{115}Sn are indicated by a, b, and c respectively in the inset. (b) Phase-cycled 1D-HMQC. (c) One-dimensional ge-HMQC spectrum using a 50:45.65:40 gradient-strength ratio.

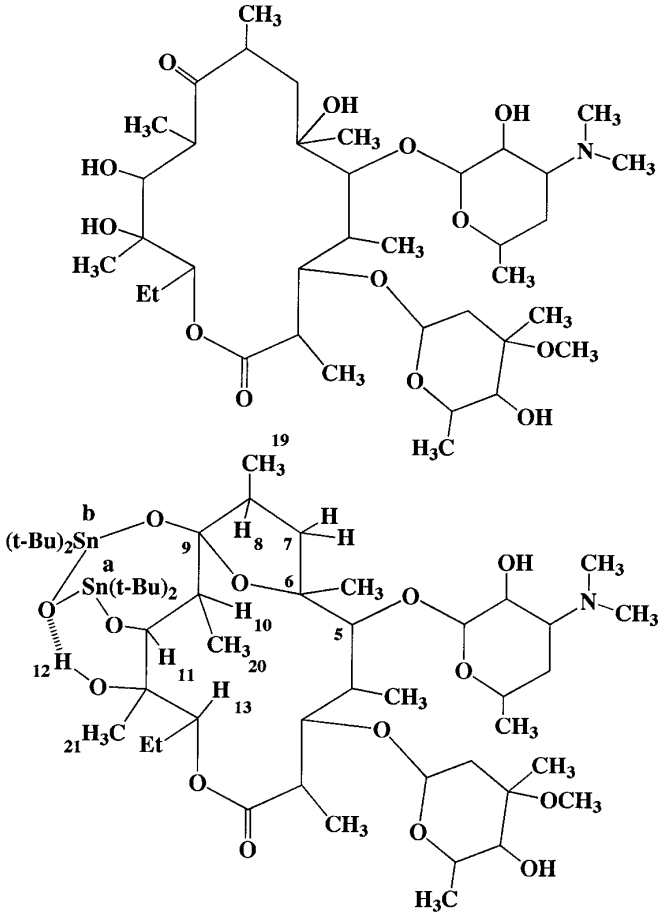

FIG. 3. Structure of erythromycin A, Ery$(OH)_2$ (top) and its Ery$(OSn(^tBu)_2)_2O$ derivative (bottom) with labeling as discussed in the text.

unwanted coherence-transfer pathways undetectable, provided sufficiently strong or long gradients are applied to achieve sufficient phase randomization over the whole sample (*18*). In this respect, the 50:45.65:40 gradient ratio is preferred to the 50:−6.291:40 ratio, as the former provides nearly twice as much dephasing for ^{119}Sn-uncoupled ^{1}H resonances, at equal gradient field strength, as verified experimentally.

Two-dimensional ge-^{1}H−{^{119}Sn} HMQC experiments covering the full range of $^nJ(^1H-^{119}Sn)$ values were performed to assess the robustness of the gradient trains against other possible artifacts discussed by Ruiz-Cabello *et al.* (*16*). Cross peaks corresponding to DQC, ZQC, or other frequencies, expected to occur because of $\pi(^1H)$ pulse inaccuracy, were absent, even when this pulse angle was set to $\pi/2$. During initial development of the ge-HMQC experiment, artifacts corresponding to axial peaks ($\omega_{119Sn} = 0$) were observed, despite the fact that both gradient trains should render the associated pathway unobservable. As it turns out, the T_2 ^{1}H relaxation times of the aromatic protons were long enough to cause part of the ^{1}H SQC dephased in the first scan to be refocused in the subsequent scan. This was confirmed by noting that the intensity of these axial peaks decreases with increasing interscan delay, and by the fact that these peaks appeared for any combination of G_1:G_2:G_3, thus demonstrating the occurrence of a gradient-recalled echo over two successive scans. Whenever this occurs, a fourth ''purging'' PFG can be added following acquisition (Fig. 1), thus preventing undesired refocusing prior to full T_2 relaxation.

As reviewed by Keeler *et al.* (*18*), the application of PFGs during t_1 causes half of the signal evolving in t_1 to be lost. As only one coherence pathway is retained, the signal is phase modulated during t_1, precluding pure-phase representation of the spectrum. This is not a major concern, however, as the evolution of homonuclear scalar couplings and proton chemical shifts during the long HMQC preparation delays used here causes the detected signal to be phase modulated anyway (*20*). For this reason, phase-cycled HMQC spectra for the detection of small scalar couplings are usually recorded with N-type signal selection followed by Fourier transformation toward an absolute value representation. The overall result is identical to that in the ge-HMQC experiment, and consequently the benefits associated with gradient enhancement are enjoyed without any reduction in signal-to-noise, provided identical numbers of scans are compared. The only possible caveat of gradient introduction is that, for ^{119}Sn nuclei with short T_2 relaxation times (possibly as a result of chemical exchange common in solution tin chemistry), the lengthening of the t_1 evolution period by the introduction of gradients may reduce the signal-to-noise ratio in the spectrum.

ge-^{1}H−{^{119}Sn} HMQC proved indispensable to elucidate the covalent structure of Ery$(OSn(^tBu)_2)_2O$. This novel tin derivative of the well-known antibiotic drug erythromycin A (Fig. 3), intended as a potential anti-tumor agent (*1*), was synthesized from a reaction mixture of erythromycin A with bis(propoxy-di-*t*-butyltin)oxide generated *in situ* (*21*) in propanol at room temperature, according to Scheme 1:

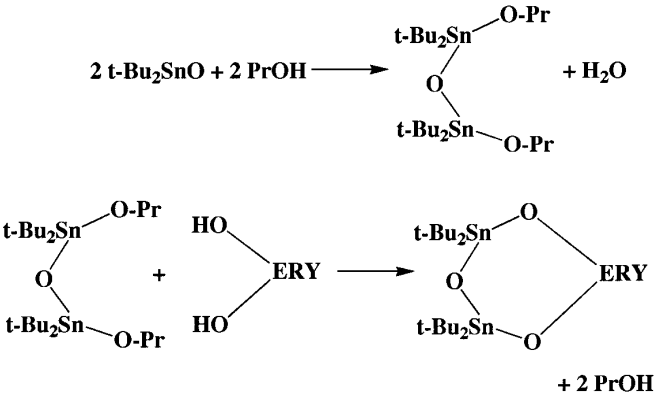

Scheme 1

The $-(^tBu)_2Sn-O-Sn(^tBu)_2-$ moiety, evidenced by the characteristic $^2J(^{119}Sn-O-^{117/119}Sn)$ coupling constant of 110 Hz in the ^{119}Sn spectrum, is incorporated between two

hydroxyl groups according to a structural pattern to be identified. Although many different compounds can potentially be formed as a consequence of the five different hydroxyl functionalities in erythromycin A, this reaction produces only one compound which, after isolation, was shown to be NMR-spectroscopically pure. Details on the synthesis as well as complete ^{1}H and ^{13}C assignments in C_6D_6, obtained from 1D ^{1}H and ^{13}C proton-decoupled DEPT-135 spectra in combination with 2D $^{1}H-\{^{13}C\}$ HMQC and HMBC experiments, will be published elsewhere. These assignments allow one to conclude that the sugar units are totally unaffected by the reaction, while the macrocycle is basically preserved. However, the $^{13}C9$ resonance has a chemical shift consistent with an acetal carbon, suggesting that the reaction involves a hemiacetal function at C9 (see below). This is retrospectively expectable as, in polar media, minor isomers of erythromycin A with acetal rings involving C9 have been described (*22–24*). The ^{119}Sn chemical shifts at -234 and -294 ppm indicate tetracoordinated di-*t*-butyl-tin atoms (*25*), referred to as Sn(a) and Sn(b) respectively.

These data do not enable one to locate the $-(^{t}Bu)_2Sn\text{-}O\text{-}Sn(^{t}Bu)_2$-moiety. Accordingly, phase-cycled 2D $^{1}H-\{^{119}Sn\}$ HMQC spectra covering the complete range of $^{n}J(^{1}H-^{119}Sn)$ coupling constants were recorded as described previously (*11*). From the F_2 cross sections through both Sn nuclei, intense correlations with $^{3}J(^{1}H-^{119}Sn)$ coupling constants from 99 to 107 Hz are observed. For Sn(a), a rather intense doublet is observed at the chemical shift of H11 (not shown). The associated coupling constant of 27 Hz, only consistent with a $^{3}J(^{1}H-^{119}Sn)$ correlation, indicates unequivocally the involvement of the 11-OH group in the above reaction, with formation of a C11–O–Sn(a) bond. In contrast, the second bond involving Sn(b) cannot be assigned from these spectra. Indeed, only long-range correlations ($n > 3$) involving Sn(b) are expected since all other hydroxyl functions potentially involved in bridge formation are tertiary. The only correlation that can confidently be identified from the trace in Fig. 4b involves H10. As $^{n}J(^{1}H-^{119}Sn)$ couplings extending over five (*13*) bonds have been demonstrated, this correlation is by itself insufficient to identify the hydroxyl function involved.

With gradient enhancement, the information quality of the $^{1}H-\{^{119}Sn\}$ HMQC spectrum increases dramatically, as can be appreciated from the corresponding trace (Fig. 4c). In addition to the correlation of Sn(b) with H10, new correlations are now evident with H11, H7, H8, and Me19. Taken together, they make it possible to identify the hemiacetalic C9 atom as the second group involved in the reaction, and not C6–OH or C12–OH, as no correlations were observed with H5 or H13. For Sn(a), correlations with H10, H13, and Me21 reinforce the assignment based on phase-cycled experiments.

From these experiments, it is also quite evident that the presence of intense signals originating from the $^{3}J(^{1}H-^{119}Sn)$ couplings with the *tert*-butyl groups obscure correlations of the ^{119}Sn nuclei with other aliphatic and methyl resonances. Habitually, the large spread in individual $^{3}J(^{1}H-^{119}Sn)$ coupling constants precludes efficient use of a low-

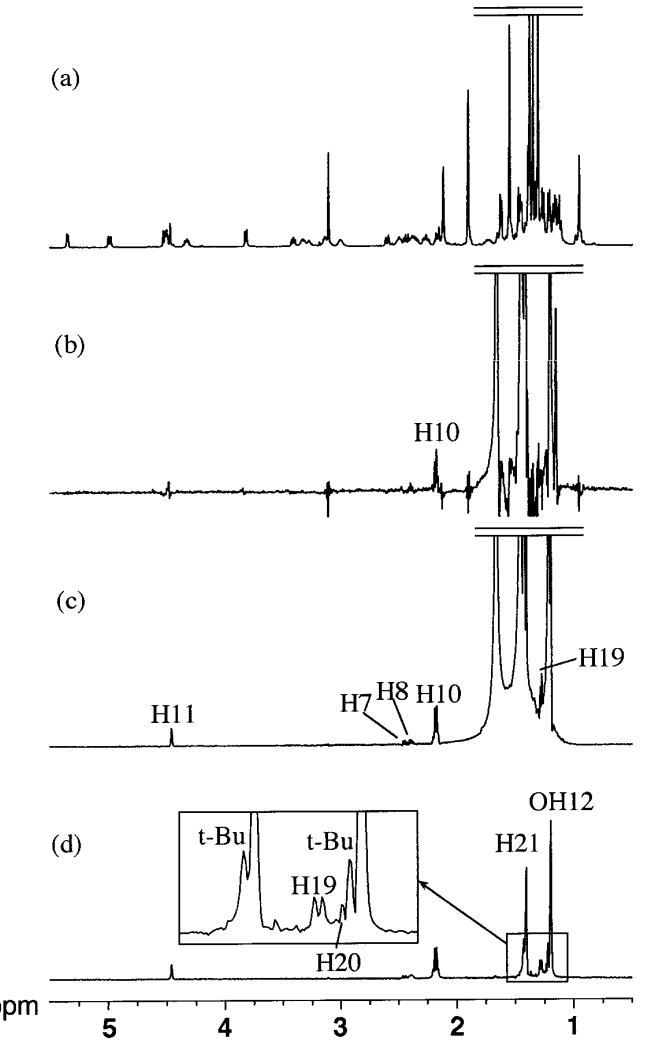

FIG. 4. One-dimensional traces corresponding to F_2 cross sections of the 2D $^{1}H-\{^{119}Sn\}$ HMQC spectrum, at the resonance frequency of Sn(b) at -294 ppm of $Ery(OSn(^{t}Bu)_2)_2O$. (a) Reference 1D spectrum. (b) One-dimensional trace from the phase-cycled HMQC spectrum. (c) One-dimensional trace from the ge-HMQC experiment recorded under identical conditions, without phase cycling, using the scheme in Fig. 1 without the additional gradient G_4. (d) One-dimensional trace from the ge-HMBC experiment (additional low-pass filter), resulting in substantial attenuation or even suppression of unwanted, very intense ^{1}H resonances from the *tert*-butyl groups. The inset shows an expansion of the resonance range of interest with the corresponding assignment. The sample consisted of 0.025 *M* $Ery(OSn(^{t}Bu)_2)_2O$ in C_6D_6. A total of 256 scans preceded by 32 dummy scans and 1 s relaxation delay were recorded, with phase cycle or gradients set to record the N-type signal. The delay for $^{n}J(^{1}H-^{119}Sn)$ evolution was set to 120 ms. A total of 128 t_1 increments were recorded. Processing consisted of zero filling in t_1, followed by squared cosine window multiplication and Fourier transformation in both dimensions. Baseline correction was needed only for the phase-cycled experiment. Long-range $^{n}J(^{1}H-^{119}Sn)$ correlations assigned with the phase-cycled experiment are given in (b). Additional unambiguous assignments from ge-HMQC and HMBC are indicated in (c, d).

pass filter to remove these, as shown previously (*10*). Since in this case, however, the various *tert*-butyl $^{3}J(^{1}H-^{119}Sn)$ couplings differ by 8 Hz at most, ge-HMBC was also performed, and the corresponding cross section for Sn(b) is shown in Fig. 4d. The effective disappearance or attenuation of the *tert*-butyl signals affords a clear-cut observation of all previously mentioned long-range $^{n}J(^{1}H-^{119}Sn)$ interactions, and reveals new interactions with Me20 and Me21, only observable here. Overall, the wealth of long-range $^{n}J(^{1}H-^{119}Sn)$ correlations observed in these experiments allows the $-(^{t}Bu)_2Sn-O-Sn(^{t}Bu)_2-$ moiety to be inserted as shown in Fig. 3.

In addition, the spectra display a correlation to the so-far undiscussed proton resonance assigned to 12-OH, which appears to be common to both Sn(a) and Sn(b) (Fig. 4d). Its hydroxylic nature is evidenced by the disappearance of its proton resonance upon addition of D_2O. Using isotope shifts observed in ^{13}C SIMPLE (*26*) experiments, this hydroxyl proton could be assigned to 12-OH, indicating that C6–OH is involved in the new acetal ring. This is supported by the striking high-frequency shift (10.9 ppm) of the ^{13}C chemical shift of C6, in contrast to the near absence of such a shift (0.7 ppm) on C12 when compared with free erythromycin. The simultaneous presence with comparable strong intensities of the $^{1}H-^{119}Sn$ correlations between the 12-OH ^{1}H resonance and the Sn(a) and Sn(b) ^{119}Sn resonances is unlikely to originate from $^{5}J(^{1}H-^{119}Sn)$ and $^{7}J(^{1}H-^{119}Sn)$ couplings. An attractive explanation is the presence of a hydrogen bond as shown in Fig. 3, a feature further substantiated by the occurrence of similar H/D SIMPLE effects on both ^{119}Sn resonances upon partial deuteration.

In conclusion, we have set up and optimized a gradient-enhanced version of the $^{1}H-\{^{119}Sn\}$ HMQC experiment, and demonstrated its much superior performance in addressing structural and conformational characteristics of organotin compounds as compared to the basic phase-cycled experiment. As a result, we expect this technique to reveal more reliably the features of the coordination sphere of tin atoms in organotin compounds. We anticipate that the investigation of organometallic compounds containing other spin-$\frac{1}{2}$ nuclei such as ^{103}Rh, ^{109}Ag, ^{113}Cd, ^{199}Hg, and ^{207}Pb, will also benefit from the advantages demonstrated here.

ACKNOWLEDGMENTS

The financial support of the Belgian National Science Foundation (FKFO, Grant 2.0094.94) and of the Belgian ''Nationale Loterij'' (Grant 9.0006.93) is acknowledged. P.V. is a postdoctoral fellow with the ''Nationaal Fonds voor Wetenschappelijk Onderzoek,'' NFWO.

REFERENCES

1. M. Gielen, (Ed.), ''Tin-Based Antitumour Drugs,'' Springer-Verlag, Berlin, 1990; M. Gielen, P. Lelieveld, D. de Vos, and R. Willem, *in* ''Metal Complexes in Cancer Therapy'' (B. K. Keppler, Ed.), p. 383, VCH, Weinheim, 1993.
2. C. Sanchez, F. Ribot, and S. Doeuff, *in* ''Organometallic Polymers with Special Properties'' (R. M. Lane, Ed.), p. 267, Kluwer Academic, New York, 1992.
3. W. R. Croasmun and R. M. K. Carlson (Eds.), ''Two-Dimensional NMR Spectroscopy. Applications for Chemists and Biochemists,'' 2nd ed., VCH, New York, 1994.
4. J. T. B. H. Jastrzebski and G. Van Koten, *Adv. Organometal. Chem.* **35,** 241 (1993).
5. E. R. T. Tiekink, *Appl. Organometal. Chem.* **5,** 1 (1991).
6. E. R. T. Tiekink, *Trends Organometal. Chem.* **1,** 71 (1994).
7. M. Gielen, A. El Khloufi, M. Biesemans, F. Kayser, R. Willem, B. Mahieu, D. Maes, J. N. Lisgarten, L. Wyns, A. Moreira, T. K. Chattopadhay, and R. A. Palmer, *Organometallics* **13,** 2849 (1994).
8. F. Kayser, M. Biesemans, A. Delmotte, I. Verbruggen, B. Mahieu, I. De Borger, M. Gielen, R. Willem, and E. R. T. Tiekink, *Organometallics* **13,** 4026 (1994).
9. F. Kayser, M. Biesemans, A. Delmotte, R. Hendrix, P. Malschaert, I. Verbruggen, B. Mahieu, R. Willem, and M. Gielen, *Bull. Soc. Chim. Belges.* **103,** 273 (1994).
10. F. Kayser, M. Biesemans, M. Gielen, and R. Willem, *J. Magn. Reson. A* **102,** 249 (1993).
11. F. Kayser, M. Biesemans, M. Gielen, and R. Willem, *in* ''Advanced NMR Applications to Organometallic Chemistry,'' ''Physical Organometallic Chemistry,'' Vol. 1, Chap. 3, Wiley, Chichester, 1996, in press.
12. F. Kayser, M. Biesemans, M. Bouâlam, E. R. T. Tiekink, A. El Khloufi, J. Meunier-Piret, A. Bouhdid, K. Jurkschat, M. Gielen, and R. Willem, *Organometallics* **13,** 1198, 4126 (1994).
13. R. Willem, A. Bouhdid, F. Kayser, A. Delmotte, M. Gielen, J. C. Martins, M. Biesemans, B. Mahieu, and E. R. T. Tiekink, *Organometallics* **15,** 1920 (1996).
14. M. Biesemans, R. Willem, S. Damoun, P. Geerlings, M. Lahcini, P. Jaumier, and B. Jousseaume, *Organometallics* **15,** 2237 (1996).
15. R. Hurd and B. K. John, *J. Magn. Reson.* **91,** 648 (1991).
16. O. Ruiz-Cabello, G. W. Vuister, C. T. Moonen, P. Van Gelderen, J. S. Cohen, and P. C. M. Van Zijl, *J. Magn. Reson.* **100,** 342 (1992).
17. R. R. Ernst, G. Bodenhausen, and A. Wokaun, *in* ''Principles of Nuclear Magnetic Resonance in One and Two Dimensions,'' p. 38, Oxford Univ. Press, Oxford, 1987.
18. J. Keeler, R. Clowes, A. L. Davis, and E. D. Laue, *Methods Enzymol.* **239,** 145 (1994).
19. A. Bax, *J. Magn. Reson.* **52,** 76 (1983).
20. A. Bax and M. F. Summers, *J. Am. Chem. Soc.* **109,** 2093 (1986).
21. G. Davies, D. C. Kleinschmidt, P. R. Palan, and S. C. Virashtha, *J. Chem. Soc. C,* 3792 (1971).
22. J. Barber, J. I. Gyi, L. Lian, G. A. Morris, D. A. Pye, and J. K. Sutherland, *J. Chem. Soc. Perkin Trans. 2,* 1489 (1991).
23. J. R. Everett, E. Hunt, and J. W. Tyler, *J. Chem. Soc. Perkin Trans. 2,* 1481 (1991).
24. J. R. Everett and J. W. Tyler, *J. Chem. Soc. Perkin Trans. 2,* 1659 (1987).
25. B. Wrackmeyer, *Annu. Rep. NMR Spectrosc.* **16,** 73 (1985).
26. J. C. Christofides and D. B. Davies, *J. Am. Chem. Soc.* **105,** 5099 (1983).